



PII S0016-7037(98)00286-5

Evaporation of single crystal forsterite: Evaporation kinetics, magnesium isotope fractionation, and implications of mass-dependent isotopic fractionation of a diffusion-controlled reservoir

JIANHUA WANG,^{1,*} ANDREW M. DAVIS,^{1,2} ROBERT N. CLAYTON,^{1,2,3} and AKIHIKO HASHIMOTO^{4,‡}¹Department of the Geophysical Sciences²The Enrico Fermi Institute³Department of Chemistry, The University of Chicago, Chicago, Illinois 60637, USA⁴Harvard-Smithsonian Center for Astrophysics, Cambridge, Massachusetts 02138, USA

(Received August 26, 1996; accepted in revised form September 9, 1998)

Abstract—Single crystals of forsterite were evaporated in a vacuum furnace at temperatures of 1500–1800°C to study evaporation kinetics, magnesium isotopic fractionation, and magnesium diffusion in forsterite. The evaporation of single crystal forsterite revealed that the evaporation process is kinetically hindered, in agreement with the results of Hashimoto (1990) on polycrystalline forsterite. The activation energy of forsterite evaporation obtained from this study is 628 kJ/mole. Forsterite can thus be much more refractory at low temperatures than expected from thermodynamic predictions.

The evaporation of solid forsterite supports a model of isotopic fractionation under diffusion-controlled conditions such that isotopic fractionation during the evaporation process is restricted to the vicinity of the evaporating surface. The measured solid-gas fractionation factor of ²⁶Mg/²⁴Mg is smaller than the theoretical prediction, suggesting more complicated gas speciation than a monatomic Mg gas. Diffusion coefficients of forsterite at high temperature (1500–1800°C) were obtained based on measurement of isotopic profiles in the evaporation residues. Mg diffusion in forsterite along its crystallographic *a*-axis has a very high activation energy (608 kJ/mole). Copyright © 1999 Elsevier Science Ltd

1. INTRODUCTION

Calcium-, aluminum-rich inclusions (CAIs) in meteorites carry important information on the physical and chemical conditions of the solar nebula. The process of evaporation has been shown to play an important role in the formation of CAIs (Kurat, 1970; Tanaka and Masuda, 1973; Chou et al., 1976; Notsu et al., 1978; Nagasawa and Onuma, 1979; Hashimoto et al., 1979; Lee et al., 1979, 1980; Hashimoto, 1983; Niederer and Papanastassiou, 1984; Clayton et al., 1988; Davis et al., 1990; Ireland et al., 1992). Among the metallic rock-forming elements with more than one stable isotope (magnesium, silicon, calcium, titanium, chromium, iron, and nickel), isotopic fractionation is small to immeasurable in ordinary chondrites, achondrites, and lunar and terrestrial rocks (except that silicon varies by about 3‰/amu in terrestrial materials, Tilles, 1961). Large isotopic fractionation of these elements has been found in some CAIs, and has been attributed to evaporation in the solar nebula.

Hashimoto (1983) emphasized the kinetic aspects of evaporation in order to characterize the rate-determining processes for each of the major elements he studied (magnesium, silicon, aluminum, calcium, and iron). He found that use of the chemical composition of the major elements alone did not allow

discrimination between evaporation and condensation evolution paths for the origin of CAIs. During equilibrium condensation or evaporation processes, isotopic fractionation is very small for silicon, magnesium, and calcium, because the difference in isotopic partition function ratios for these elements between gas and condensed phase is extremely small at high temperatures. However, heavy-isotope enrichment (up to a few percent per amu) is found in magnesium, silicon, oxygen, titanium, and calcium in CAIs (Clayton et al., 1988). This enrichment results from the kinetic isotope effect between vapor and liquids or solids due to nonequilibrium evaporation of the precursor material (Davis et al., 1990). Thus, stable isotope fractionation effects can be used to distinguish between evaporation and condensation processes.

Evaporation from a crystalline surface produces a kinetic isotope effect in which light isotopes of each evaporating species evaporate at a greater rate than heavy isotopes. The resulting heavy-isotope enrichment at the surface of the solid then propagates into the crystal by diffusion. Thus, measurements of evaporation rates and of the isotopic diffusion profile in the residual crystal can yield both the magnitude of the fractionation effect and the diffusion coefficient for each element. This paper describes the application of this method to magnesium isotopes in the evaporation of single-crystal forsterite (Mg₂SiO₄).

1.1. Evaporation

Molini-Velsko et al. (1987) reported silicon isotopic analyses of evaporation residues produced by heating basalt and two carbonaceous chondrites in a solar furnace. They found that the residues were enriched in the heavy isotopes of silicon by about

*Author to whom correspondence should be addressed (Department of Terrestrial Magnetism, Carnegie Institution of Washington, Washington, DC 20015).

†Present address: Department of Terrestrial Magnetism, Carnegie Institution of Washington, Washington, DC 20015.

‡Present address: Department of the Earth and Planetary Sciences, Hokkaido University, Kita-ku, Sapporo 060, Japan.

+1.1 to +1.8‰ per amu after 80% evaporation of the original sample. Davis et al. (1990) studied residues from melts of forsterite composition evaporated under vacuum and showed that the isotopic compositions of the residues follow a Rayleigh law with fractionation factors close to the inverse square-root of molecular masses. Davis et al. also showed that forsterite evaporated from the solid state showed no measurable bulk isotopic fractionation effects. Wang et al. (1991, 1993) examined magnesium isotope profiles in forsterite residues evaporated from the solid state and found that isotopic fractionation is a diffusion-controlled process during the evaporation of solid forsterite (solid forsterite is a poorly mixed reservoir). Uyeda et al. (1991) used a Rayleigh law to explain isotopic fractionation in both residue and condensates by evaporating forsterite in the solid state under vacuum. Using coarse-grained forsterite (>200 μm) as the evaporation source, they found that $\delta^{26}\text{Mg}$ in the residues was enriched by <3‰ even after two-thirds of the initial mass had been evaporated.

Previous investigations showed that forsterite evaporates congruently (the chemical composition of the residue remains the same) both from the solid and the liquid state under either equilibrium or kinetic conditions (Mysen and Kushiro, 1988; Nagahara et al., 1988; Hashimoto, 1990; Nagahara and Ozawa, 1996). Mysen and Kushiro (1988) measured the equilibrium vapor pressure of forsterite under different oxygen fugacities by the Knudsen method. They found that the evaporation rate of forsterite is independent of oxygen fugacity within experimental error. Nagahara et al. (1994) remeasured the vapor pressure of forsterite using the same experimental setup as Mysen and Kushiro (1988) and obtained the enthalpy and entropy of evaporation of forsterite. Using their equilibrium phase relations, they explained that the difference in the origin of type IA (Fe-poor) and type II (Fe-rich) chondrules was due to their formation at different olivine gas pressures. Hashimoto (1990) examined evaporation kinetics of polycrystalline forsterite under close to free evaporation conditions using a high temperature vacuum furnace, and found that Mg, SiO_2 and O (or O_2) are the rate-determining gas species during forsterite evaporation. He also pointed out that at 1700°C, Mg_2SiO_4 evaporates about one-tenth as fast as predicted from equilibrium thermodynamics with no kinetic barriers impeding the process. As the result of this kinetic effect, Mg_2SiO_4 may evaporate at the same rate as an intrinsically more refractory material. Wang et al. (1993) reported the evaporation kinetics of single crystal forsterite instead of polycrystalline forsterite as Hashimoto (1990), Davis et al. (1990) and Wang et al. (1991) had used. As the effective surface area of the polycrystalline forsterite is very difficult to determine accurately, the single crystal study provides a more accurate measurement of the forsterite evaporation kinetics.

Both Rees (1969) and Eberhardt et al. (1964) measured isotope ratios as a function of time in a thermal ionization mass spectrometer. These data show an initial increase in the ratio of the heavy to light isotopes, followed by a relatively long flat period and another increase as the sample on the filament diminishes. Eberhardt et al. (1964) pointed out that the initial enrichment of isotope ratios was not understood. Rees (1969) derived the following equation to describe this isotopic fractionation:

$$\Delta(x) = (1 - \alpha)(1 - e^{-x/D}), \quad (1)$$

where $\Delta(x)$ is the isotopic composition of the mixed layer extending from depth x to depth $x + D$, α is the isotopic fractionation factor between the vapor phase and the residual phase, and D is the thickness of the mixed layer near the evaporating surface. With the thickness of the mixed layer D unconstrained, it is very difficult to use this formula quantitatively. A treatment of this problem, including diffusion control, is given in Appendix A.

1.2. Diffusion

Diffusion plays an important role in controlling magnesium isotopic fractionation during the evaporation of solid forsterite (Wang et al., 1991, 1993). There are four major mechanisms related to volume diffusion in a crystal (see Manning, 1974 for details): (1) interchange of two neighboring atoms in the crystal lattice (exchange mechanism); (2) moving of interstitial atoms from one interstitial site to another (interstitial mechanism); (3) movement of vacancies in the crystal structure (vacancy mechanism); and (4) pushing a normal lattice atom into an interstitial site by replacing it with an interstitial atom (interstitialcy mechanism). Different mechanisms usually have different activation energies and may control diffusion rates over different temperature ranges. Buening and Buseck (1973) showed that iron-magnesium interdiffusion in olivine changes at 1125°C to a higher activation energy process, indicating more than one diffusion mechanism. Another complication for the study of diffusion is anisotropy of the crystal, such as Clark and Long (1971) observed for nickel diffusion in olivine (Fo_{94}). The chemical diffusion coefficient of nickel in olivine is an order of magnitude greater along the c -axis than along the a - and b -axes over the temperature range 1149–1234°C. They found that this anisotropy in diffusion coefficients decreases with increasing temperature. Anisotropy in diffusion was also detected for iron-magnesium interdiffusion in olivine (Buening and Buseck, 1973). Morioka (1980) observed similar anisotropy of cobalt-magnesium interdiffusion in olivine. Chakraborty et al. (1994) measured the self-diffusion of Mg in synthetic single crystal forsterite from 1000 to 1300°C and found that at 1100°C, diffusion along the c -axis is four times faster than along the a -axis and six times faster than along the b -axis. They also found the diffusion coefficient to be only a weak function of oxygen fugacity at 1100°C. The anisotropy of oxygen diffusion in forsterite is very small to almost undetectable, within experimental resolution (Jaoul et al., 1983). Our knowledge of magnesium diffusion in forsterite is rather limited and spans a relatively narrow temperature range (Hallwig et al., 1980; Morioka, 1981; Chakraborty et al., 1994).

In this study, we present measurements of magnesium isotope fractionation occurring in the irreversible evaporation of single-crystal forsterite. The experimental results obtained are: (1) the evaporation rate as a function of temperature, (2) the self-diffusion coefficient of magnesium in forsterite as a function of temperature, and (3) the isotopic fractionation factor of the evaporation process. These data permit determination of the molecular speciation of the vapor in the rate-controlling step. The diffusion coefficients apply at higher temperatures than

those measured previously, and are important for terrestrial mantle processes.

2. EXPERIMENTAL AND ANALYTICAL METHODS

2.1. Vacuum Furnace

The evaporation experiments were conducted in a vacuum furnace designed and built by Akihiko Hashimoto at the Harvard-Smithsonian Astrophysical Observatory (Hashimoto, 1990) and now located at the University of Chicago. The furnace chamber is cylindrical, with a height of 46 cm and a diameter of 36 cm. In the center is a pair of vertically mounted hemicylindrical tungsten mesh resistance heaters (about 15 cm high and 2.5 cm in diameter). Outside the heaters is a seven-layer, tungsten-molybdenum thermal radiation shield to keep the hot zone at a uniform temperature, surrounded by a water-cooled stainless steel insulator. Five holes ~2 cm in diameter on the top, bottom, front and two sides of the radiation shield allow the efficient evacuation of the vapor generated from the sample during the evaporation process. The furnace is equipped with a 260 liter s⁻¹ Welch turbomolecular pump and can maintain a pressure of 1 × 10⁻⁶ Torr with the furnace at 2500°C. Two W₁₀₀/W₇₄Re₂₆ thermocouples about 15 mm apart were used to measure the temperature of the hot zone in the furnace. The heating process was programmed and controlled automatically with a Eurotherm 818 temperature control system using one of the thermocouples. A one-color Pyro microoptical pyrometer was also used occasionally to measure the temperature by aiming at the inside bottom of a graphite tube open at one end (15 mm long, 12 mm deep, 2 mm inside diameter) mounted between the two thermocouples. The estimated accuracy of temperature measurement is ±3°C. The vertical variation of temperature in the center of the furnace is estimated to be <5°C within 10 mm of the thermocouples. The sample was placed about 5 mm above the graphite tube and the thermocouples.

The gas evacuation rate from the sample vicinity (inside the radiation shield) to the main vacuum chamber can be calculated from gas flow theories (see Dushman, 1961 for details). For an ideal gas under the molecular flow condition (in which the Knudsen number, the ratio of the mean free path to the dimension of the gas flow channel, is >1), the conductance of a short cylindrical tube can be obtained from the following equation:

$$F = \frac{\pi d^3}{4d + 3l} \sqrt{\frac{RT}{2\pi M}}, \quad (2)$$

where d is the diameter and l the length of the tube, R is the gas constant, T the absolute temperature, and M the molecular weight of the flowing gas (after Dushman, 1961). The calculated gas conductance of the Hashimoto furnace configuration is 36.6√ T/M liter s⁻¹, where T is in Kelvin and M in g mole⁻¹. The number of gas molecules of the evaporating sample (assuming a single species for simplicity) inside the radiation shield is controlled by both the rate of evacuation of the gas through the holes in the shield and the rate of evaporation of the sample. If the sample gas pressure outside the radiation shield is assumed to be zero and the sample is assumed to be evaporating at its maximum rate, the following formula gives the rate of accumulation of the sample gas molecules inside the shield:

$$\frac{dn}{dt} = \frac{P_e A}{\sqrt{2\pi R M T_s}} - \frac{F P_i}{R T_g}, \quad (3)$$

where P_e is the thermodynamic equilibrium gas pressure of the sample at temperature T_s with surface area A and molecular weight M , F the gas conductance (from inside the radiation shield to outside the cooling water jacket), P_i the sample gas pressure inside the shield (assumed uniform) and T_g the gas temperature. Using the ideal gas law to relate n to P_i , V (volume inside the shield), and T_g , Eq. 3 can be integrated and yields:

$$\frac{P_i}{P_e} = \sqrt{\frac{R}{2\pi M T_s}} \frac{A T_g}{F} (1 - e^{-(F/V)}). \quad (4)$$

The sample surface area has been assumed to be constant, which should not be too critical if the average surface area is used. P_i/P_e is the

fraction of the gas that collides with the sample after evaporation and will be defined as collision factor R_c . R_c is thus an indicator of reprecipitation. Although Eq. 4 is based on the thermodynamic equilibrium pressure P_e , P_e can be replaced by any other kind of pressure that reflects the evaporation rate. Eq. 4, with the substitution of R_c for P_i/P_e , can be used to study the reprecipitation for any kind of kinetic evaporation process. Steady state will be reached when the evacuation rate equals the evaporation rate. For all of our evaporation experiments, steady state should be reached in a few seconds. At steady state, R_c becomes maximum and is shown if $T_g = T_s = T$ is assumed for simplicity:

$$R_c^{\text{steady}} = \sqrt{\frac{RT}{2\pi M}} \frac{A}{F}. \quad (5)$$

Thus R_c^{steady} is 0.099A (A in cm²), assuming that the pressure of the evaporating material in the main vacuum chamber is zero. Since the temperature of the gas leaving the shield is lower than the temperature of the sample, this calculated R_c^{steady} sets the upper limit of R_c . This means that >90% of the vapor produced during the evaporation will never come back to collide with the sample with a surface area of 1 cm².

2.2. Evaporation Procedures

Dr. Robert C. Morris of Allied Signal Corp. provided a large piece of forsterite single crystal (with Co/(Co + Mg) = 0.001) for the evaporation experiments. The crystal was sliced into disks (~10 mm in diameter and 1 mm thick) perpendicular to the a -axis of the crystal and polished on both surfaces. Forsterite chips were hung in the center of the heater ~5 mm above the thermocouple by means of a three-leg tungsten or iridium wire hanger. After the sample was loaded in the furnace, the furnace chamber was evacuated and baked at 120°C for 2–3 h. Overnight pumping reduced the pressure in the furnace to about 5 × 10⁻⁷ Torr. Heating rates of 20°C min⁻¹ initially and 100°C min⁻¹ later were used to keep the furnace under desired vacuum. When the prescribed duration of the evaporation at specified temperature was reached, the heater power was turned off to quench the reaction. The radiation cooling rate of the furnace is >200°C min⁻¹ during the first 3 min of cooling from 1750°C.

A total of 23 evaporation runs were performed at temperatures from 1500 to 1800°C with different degrees of evaporation in the vacuum furnace. Of these, 17 were sufficiently free of surface irregularities to be used for determination of evaporation rates; 13 specimens were used for measurement of isotopic profiles. The weight and the surface area of each chip were measured before and after the evaporation run to determine the evaporation rate. The weight measurement was accurate within 0.1 mg. The shapes of the forsterite chip were not regular (some edges were curved, some were quadrilateral polygons and others triangles). The accuracy of determination of the total surface area was within a few square millimeters (<1% relative). The average surface area was determined from measurements before and after evaporation and corrected for the change of surface area with time.

The experimental conditions and the evaporation results are summarized in Table 1. The samples were weighed with a precision of ±0.1 mg; the weighing error should cause <2% error in the evaporation rate (except for FS13 with 4%, which was not included in the final result). The estimate of surface area by assuming a perfectly flat surface is accurate to ±3 mm². This could introduce an error of 0.6–3.5% to the calculation of the evaporation rate.

2.3. Mg Isotopic Analysis of Forsterite Residues

A modified AEI IM-20 ion microprobe (Banner and Stimpson, 1974; Scatena-Wachel, 1986) was used to measure magnesium isotopic compositions in the evaporation residues. The primary beam of 20 keV ¹⁶O⁻ ions was focused to a 10 μm spot. Secondary ions were mass analyzed at a resolution ($M/\Delta M$) of 300, as there are no significant isobaric interferences at $m/e = 24, 25$, or 26 (except for hydrides; see below). Isotopic abundances were determined by ion counting; typical ²⁴Mg count rates were ~5 × 10⁵ counts s⁻¹; the system deadtime was 22 ns, and background was 0.02 counts s⁻¹.

Sections perpendicular to the evaporating surface of the residues

Table 1. Summary of single crystal forsterite evaporation experiments.

Run #	Temperature (°C)	Duration (h)	Initial wt. (g)	Final wt. (g)	Percent evaporated	Surface area (cm ²)	Evaporation rate (mole cm ⁻² s ⁻¹)
FS13	1500	24	0.0904	0.0880	2.65	0.880	2.24×10^{-10}
FS14	1500	48	0.1833	0.1780	2.89	1.562	1.40×10^{-10}
FS15	1500	96	0.1824	0.1717	5.87	1.643	1.34×10^{-10}
FS6	1600	16	0.3825	0.3580	6.41	2.475	1.22×10^{-9}
FS26	1600	24	0.2827	0.2566	9.23	2.222	9.66×10^{-10}
FS7	1600	32	0.3497	0.3105	11.21	2.105	1.15×10^{-9}
FS16	1600	32	0.1756	0.1428	18.68	1.635	1.24×10^{-9}
FS22	1680	12	0.1975	0.1322	33.06	1.709	6.29×10^{-9}
FS23	1680	24	0.1725	0.0611	64.58	1.471	6.23×10^{-9}
FS21	1750	3	0.0882	0.0561	36.39	0.862	2.45×10^{-8}
FS24	1750	5	0.1713	0.0904	47.23	1.389	2.30×10^{-8}
FS18	1750	8	0.1316	0.0241	81.69	1.088	2.44×10^{-8}
FS10	1800	1	0.4154	0.3400	18.15	2.389	6.23×10^{-8}
FS20	1800	1	0.0903	0.0613	32.12	0.930	6.16×10^{-8}
FS25	1800	2	0.1654	0.0905	45.28	1.320	5.60×10^{-8}
FS11	1800	3	0.3123	0.1381	55.78	1.909	6.00×10^{-8}
FS12	1800	4.5	0.5108	0.1548	69.69	2.678	5.83×10^{-8}

were mounted in epoxy and polished for electron microprobe and ion microprobe analysis. Electron microprobe profiles with 1 μm spacing did not show any measurable variations in the Mg/Si ratio across entire sections. Detailed ion microprobe determination of magnesium isotopic compositions across these sections did not reveal any isotopic fractionation profiles or systematic changes. Because of the limited spatial resolution of the ion microprobe ($>10 \mu\text{m}$) it was impossible to detect the isotopic profile associated with the fractionation at the evaporating surface in cross-section sample mounts.

In order to improve spatial resolution, magnesium isotopic profiles perpendicular to the evaporating surfaces of the residues were measured by depth profiling with the ion microprobe. The primary beam was rastered over an area of $\sim 100 \times 100 \mu\text{m}$ with an intensity of 30–35 nA. In order to obtain a depth profile of only the central, flat-bottomed area of the rastered pit, a digital aperture was used to collect signal from the central 52% or 25% of the total rastered area. This procedure is necessary to ensure correspondence between the depth and the isotopic data collected. In each measurement, signal collection was begun 2 min after turning on the primary beam to allow the Mg^+ signal to stabilize. Each measurement of 500–1000 cycles through ^{26}Mg , ^{25}Mg , and ^{24}Mg took 5–7 h and sampled the rastered area to a depth of $\sim 10 \mu\text{m}$. Depth profiles of single-crystal forsterite starting material were measured before and after each isotope profile of a residue in order to standardize the results and correct for instrumental drift. Several analyses of forsterite starting material show a constant magnesium isotopic composition with depth (or time). $^{25}\text{Mg}/^{24}\text{Mg}$ and $^{26}\text{Mg}/^{24}\text{Mg}$ ratios are measured with similar precision, but $^{26}\text{Mg}/^{24}\text{Mg}$ ratios have better precision on a $\%/\text{amu}$ basis. ^{25}Mg is also potentially subject to a ^{24}MgH interference. For these reasons, we report only ^{26}Mg profiles.

The depth of each rastered pit was measured using a Sloan DEKTAK surface profiler with a precision of $\pm 0.1 \mu\text{m}$. Several depth profiles across the crater perpendicular to both edges were obtained. The depth used in the diffusion coefficient calculation is the average of these different profiled depths. Each pit was also checked to see if it had a flat bottom. Those pits that did not have a flat bottom were not used. To correlate the isotopic composition with depth, the sputtering rate was assumed to be linearly proportional to the ^{24}Mg counts. The fluctuation of the primary beam intensity can thus be corrected. The results of all acceptable $\delta^{26}\text{Mg}$ profiles are listed in Table 2.

3. RESULTS AND DISCUSSION

3.1. Forsterite Evaporation Kinetics

The average evaporation rate of synthetic forsterite at each temperature is listed in Table 3. The error is estimated either from the standard deviation of repeated runs at the same tem-

perature or from the combination of errors in the weighing and the surface area determination. The actual uncertainty is probably larger due to crystal surface defects that we are unable to assess. For future experiments on kinetic evaporation of solid materials, it is important to anneal the sample to remove these surface defects before conducting the evaporation experiments, so that more accurate information on the evaporation kinetics can be obtained. The results of the evaporation of polycrystalline forsterite (extrapolated to the present temperatures from the fit to the data of Hashimoto, 1990) are also listed in Table 3 for comparison. To better illustrate these results, Fig. 1 shows the variation of the evaporation rates with temperature. All of the measured evaporation rates for single crystal forsterite are lower than those measured by Hashimoto (1990), especially at lower temperatures (Fig. 1). The ratio of the evaporation rate of the single crystal forsterite to that of the polycrystalline forsterite (relative to the fit to the data of Hashimoto, 1990) ranges from 0.61 at 1500°C to 0.85 at 1800°C (Table 3). This discrepancy is apparently the result of an underestimate of the surface area in the evaporation of the polycrystalline forsterite. Scanning electron microscopy (SEM) study of the evaporation residues of polycrystalline forsterite indicates that these residues are rather porous and that the porosity (and surface area) decreases with increasing evaporation temperature. This agrees with our observation that evaporation rates of single crystal forsterite and polycrystalline forsterite deviate more from one another at lower temperatures (Table 3 and Fig. 1). Nagahara and Ozawa (1996) reported an evaporation rate of 7.1×10^{-9} mole $\text{cm}^{-2} \text{s}^{-1}$ for forsterite at 1700°C under vacuum, which is about 25% less than that interpolated from our experiments ($9.30 \pm 0.46 \times 10^{-9}$ mole $\text{cm}^{-2} \text{s}^{-1}$).

Thermodynamic data can be used to calculate the equilibrium partial pressures of different gas species above forsterite as a function of temperature. From the equilibrium partial pressures, the rates of impingement of these gas species on a surface can be obtained using Eq. A1 (see Appendix A). Following Hashimoto (1990), the overall maximum evaporation rate, J_e , is calculated from the partial pressures of all possible species that can coexist with forsterite. For the tem-

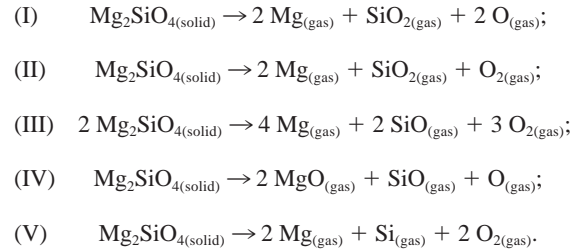
Table 2. Results from magnesium isotopic profiles.

Analysis #	T (°C)	Depth (μm)	$-v/D$	$\ln(1000(\alpha - 1))$	D ($\text{cm}^2 \text{s}^{-1}$)	α
FS15UA	1500	7.01	-0.346	3.26	1.69×10^{-12}	1.0259
FS5BA1	1600	9.06	-0.341	3.36	1.61×10^{-11}	1.0287
FS5TA1	1600	8.39	-0.355	3.34	1.55×10^{-11}	1.0282
FS6BA1	1600	7.34	-0.341	3.39	1.61×10^{-11}	1.0297
FS6TA1	1600	7.03	-0.380	3.21	1.45×10^{-11}	1.0247
FS6BB	1600	7.07	-0.417	3.35	1.32×10^{-11}	1.0285
FS6TB	1600	8.19	-0.580	3.33	9.49×10^{-12}	1.0279
FS7TB2	1600	9.93	-0.449	3.39	1.23×10^{-11}	1.0296
FS7TB3	1600	8.44	-0.476	3.31	1.15×10^{-11}	1.0274
FS7TD	1600	9.29	-0.367	3.29	1.50×10^{-11}	1.0268
FS7BB	1600	7.54	-0.541	3.24	1.02×10^{-11}	1.0255
FS16UB	1600	6.57	-0.433	3.44	1.27×10^{-11}	1.0311
FS2BA1	1750	7.34	-0.325	3.45	3.23×10^{-10}	1.0315
FS2TA1	1750	7.85	-0.339	3.41	3.09×10^{-10}	1.0303
FS2BB	1750	8.09	-0.415	3.59	2.53×10^{-10}	1.0362
FS2TB	1750	8.47	-0.336	3.56	3.12×10^{-10}	1.0352
FS3BA1	1750	7.59	-0.286	3.43	3.66×10^{-10}	1.0308
FS3TA1	1750	8.28	-0.333	3.36	3.15×10^{-10}	1.0288
FS3TA2	1750	8.09	-0.322	3.43	3.26×10^{-10}	1.0308
FS3BB	1750	6.99	-0.455	3.45	2.31×10^{-10}	1.0315
FS4BB1	1750	7.81	-0.380	3.57	2.76×10^{-10}	1.0355
FS18UA	1750	6.29	-0.331	3.40	3.17×10^{-10}	1.0301
FS21UA	1750	6.21	-0.457	3.32	2.30×10^{-10}	1.0275
FS10BA2	1800	9.36	-0.461	3.32	5.53×10^{-10}	1.0278
FS10TA1	1800	7.66	-0.387	3.34	6.58×10^{-10}	1.0283
FS10TA2	1800	9.64	-0.466	3.17	5.48×10^{-10}	1.0239
FS19UB	1800	7.76	-0.359	3.46	7.11×10^{-10}	1.0319
FS20UA	1800	6.26	-0.484	3.34	5.26×10^{-10}	1.0282

perature range in this work and using the thermodynamic data of Chase et al. (1985), the only species with significant calculated partial pressures are $\text{Mg}_{(\text{g})}$, $\text{MgO}_{(\text{g})}$, $\text{SiO}_{(\text{g})}$, $\text{SiO}_{2(\text{g})}$, $\text{O}_{(\text{g})}$ and $\text{O}_{2(\text{g})}$. For example, at 2000 K (1727°C), the total equilibrium vapor pressure above forsterite is 5.77×10^{-6} bar, with the following partial pressures: P_{Mg} , 2.38×10^{-6} bar; P_{MgO} , 1.34×10^{-8} bar; P_{SiO} , 1.18×10^{-6} bar; P_{SiO_2} , 1.71×10^{-8} bar; P_{O} , 7.88×10^{-7} bar; and P_{O_2} , 1.39×10^{-6} bar. $\text{Si}_{(\text{g})}$ was also calculated, but its partial pressure is only 8.68×10^{-15} bar at 2000 K. These partial pressures correspond to collision rates of 4.73×10^{-7} , 2.06×10^{-9} , 1.74×10^{-7} , 2.16×10^{-9} , 1.93×10^{-7} , and 2.40×10^{-7} mole $\text{cm}^{-2} \text{s}^{-1}$ for $\text{Mg}_{(\text{g})}$, $\text{MgO}_{(\text{g})}$, $\text{SiO}_{(\text{g})}$, $\text{SiO}_{2(\text{g})}$, $\text{O}_{(\text{g})}$ and $\text{O}_{2(\text{g})}$, respectively. The reversal of the evaporation reaction is the condensation reaction. The condensation coefficient η_c is defined as the ratio of the observed condensation rate to the collision rate. If only condensation on a forsterite substrate is considered, rather than condensation in the gas phase, then the gas species with the slowest impingement rate in terms of stoichiometric proportion sets the upper limit to this collision rate (and the maximum condensation rate). For the calculation above, the total impingement rates of Mg-, Si-, and O-bearing species are 4.75×10^{-7} , 1.76×10^{-7} , and 8.53×10^{-7} mole $\text{cm}^{-2} \text{s}^{-1}$. However, a forsterite molecule needs 4 atoms of O, 2 atoms of Mg and one Si atom, so the overall maximum condensation rate is controlled by Si-bearing gas phase species at 2000 K and is 1.76×10^{-7} mole $\text{cm}^{-2} \text{s}^{-1}$. At equilibrium the condensation rate and the evaporation rate must be equal by definition. Hence the overall maximum evaporation rate, J_e^- , is identical to the overall maximum condensation rate.

Specific maximum evaporation rates, J_e^- , can also be calcu-

lated from thermodynamic data for specific reactions; we have done so for the ones listed below:



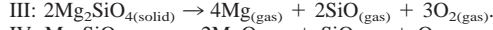
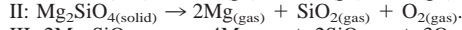
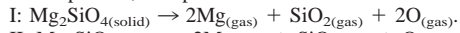
This list is not exhaustive, but represents a range of plausible reaction products, which must be compatible with both the observed overall evaporation rate and the isotopic fractionation factors.

Using these maximum evaporation rates, the forsterite evaporation coefficients η_v , defined as the ratio of the observed evaporation rate (J_v) to the maximum possible rate (J_e or J_e^-) of evaporation at equilibrium vapor pressure, were obtained and are listed in Table 3. Henceforth, we will refer to those relative to the overall maximum evaporation rate as overall evaporation coefficients and those for a specific reaction as specific evaporation coefficients. These η_v provide two kinds of information: (1) any evaporation reaction with $\eta_v > 1$ is not allowed, from the definition of η_v ; (2) the smaller the η_v , the greater the kinetic hindrance of the reaction. The overall maximum possible evaporation rate (J_e) as well as maximum evaporation rates (J_e^-) for the five specific forsterite evaporation reactions are also plotted in Fig. 1 to illustrate these two points. These data help in understanding which evaporation

Table 3. Evaporation parameters for synthetic single crystal forsterite.

Temperature (°C)	1500	1600	1680	1750	1800
Evaporation rate (mole cm ⁻² s ⁻¹)					
This study	$1.4 \pm 0.1 \times 10^{-10}$	$1.1 \pm 0.1 \times 10^{-9}$	$6.3 \pm 0.1 \times 10^{-9}$	$2.4 \pm 0.1 \times 10^{-8}$	$6.0 \pm 0.1 \times 10^{-8}$
Hashimoto*	2.25×10^{-10} *	1.96×10^{-9}	8.70×10^{-9} *	3.02×10^{-8} *	6.89×10^{-8}
Ratio	0.61	0.61	0.72	0.79	0.85
γ_v					
J_v/J_e	0.038	0.053	0.074	0.097	0.12
J_v/J_e^- (I)	0.15	0.20	0.28	0.35	0.42
J_v/J_e^- (II)	0.12	0.16	0.21	0.27	0.32
J_v/J_e^- (III)	0.042	0.058	0.081	0.11	0.13
J_v/J_e^- (IV)	1.1	1.1	1.3	1.4	1.4
J_v/J_e^- (V)	3.2	3.6	4.3	4.9	5.5
E_v (kJ mole ⁻¹)					
This study	628 ± 16				3.9×10^8
Hashimoto*	584 ± 28				3.6×10^7
Ryerson et al. (1989)	600				not available
Equilibrium (overall)	503				2.4×10^6
I	514				1.3×10^6
II	517				2.0×10^6
III	503				2.1×10^6
IV	594				3.8×10^7
V	563				1.6×10^6

* extrapolated, interpolated or fit from the data of Hashimoto (1990) for solid forsterite.



reaction is involved (or is more likely to occur) in an experimental (or natural) process. Since the evaporation rate of forsterite is much higher than the maximum rate calculated from the equilibrium thermodynamic data ($\eta_v > 1$) for evaporation reaction V, the possibility of this reaction can be excluded for the forsterite evaporation. The overall maximum evaporation rate, which by definition produces the most stable products, is much greater than that experimentally determined ($\eta_v \ll 1$); reaction III has a specific maximum evaporation rate that is nearly as high. Reaction III must be kinetically hindered. At this time it is not certain whether reaction III is kinetically restricted so as to explain the small evaporation rate determined by the experiments or reaction III is so hindered that it does not contribute to the total evaporation rate (Hashimoto, 1990). For evaporation reaction IV, almost all the experimental values are higher than the theoretical calculations ($\eta_v > 1$), but η_v is too close to one, especially at lower temperatures, to allow conclusive rejection of this possibility. For vacuum evaporation of pure MgO (periclase), Hashimoto (1990) obtained an evaporation rate that was approximately one-third of the overall maximum evaporation rate but was larger by >1 order of magnitude than the rate expected if $\text{MgO}_{\text{g}(\text{gas})}$ were involved in the specific evaporation reaction. From this result, he concluded that the major magnesium-bearing species was $\text{Mg}_{\text{g}(\text{gas})}$. This result is not inconsistent with the presence of $\text{MgO}_{\text{g}(\text{gas})}$ in the vapor phase, although its abundance should not be as high as that of $\text{Mg}_{\text{g}(\text{gas})}$. As will be discussed in the application of the

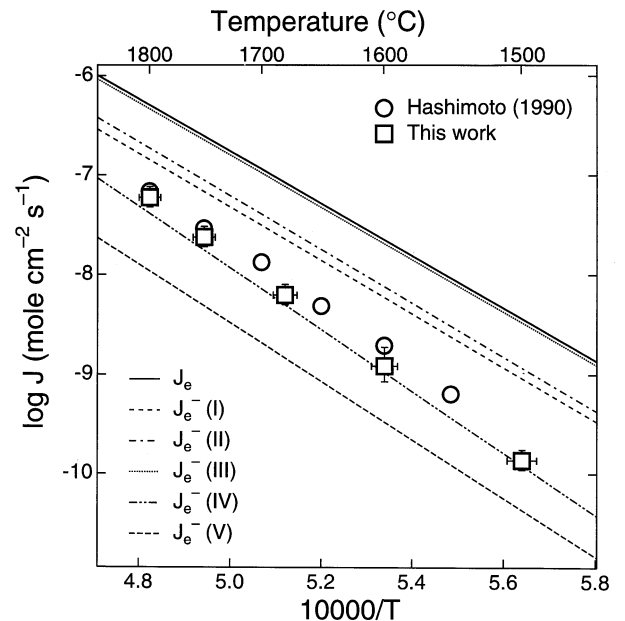


Fig. 1. Evaporation rate of synthetic single crystal forsterite (J) in vacuum versus temperature (T in Kelvin) compared with that of polycrystalline forsterite (Hashimoto, 1990). The evaporation rates of five possible evaporation reactions calculated from the thermodynamic data of Chase et al. (1985) are shown for reference.

magnesium isotopic fractionation factor to determine the evaporating gas species, $\text{MgO}_{(\text{gas})}$ may be involved in the evaporation process. Alternatively, the specific maximum evaporation rates predicted from reactions I and II are higher ($\eta_v < 1$) and closer to the experimentally obtained rates. This suggests that these two reactions are more likely to be the dominant evaporation modes, as Hashimoto (1990) proposed. Information about evaporating gas species is also provided by the study of the isotopic fractionation during the evaporation process (Wang et al., 1993, 1994a,b,c) as will be discussed later.

The temperature dependence of the evaporation rate (J_v) can be described by the Arrhenius relation:

$$J_v = J_0 e^{-E_v/RT}, \quad (6)$$

where J_0 is the preexponential evaporation rate and E_v is the activation energy of the evaporation. For the evaporation of single crystal forsterite between 1500 and 1800°C, the activation energy is 628 ± 16 kJ/mole and J_0 is 3.9×10^8 mole cm^{-2} s^{-1} (Table 3). Also listed in Table 3 for comparison are E_v (584 ± 28 kJ/mole) and J_0 (3.6×10^7 mole cm^{-2} s^{-1}) calculated from the results of polycrystalline forsterite evaporation of Hashimoto (1990). Ryerson et al. (1989) heated synthetic forsterite in a gas mixture of 5% H_2 and 95% Ar at 1300°C and a total pressure of 50 kPa to study the evaporative loss of forsterite. Combined with the result of Durham et al. (1979) for similar experiments at 1700 and 1750°C, Ryerson et al. (1989) obtained an activation energy of 600 kJ mole^{-1} . All these experimental values are in good agreement with each other in terms of the activation energy, but are higher than the theoretical calculation (503 kJ/mole) for the maximum evaporation rate (Table 3). This indicates that there is some kinetic hindrance to the forsterite evaporation process ($\eta_v < 1$) and that this hindrance (η_v) is temperature-dependent.

If forsterite evaporates to the most thermodynamically stable species, then

$$\eta_v = 161.8 \times e^{-124846/RT}. \quad (7)$$

With this equation, the deviation of the forsterite evaporation rate from thermodynamic predictions for lower temperatures can be calculated. At 1400°C η_v is 0.012, i.e., forsterite evaporates at about 1% of the rate expected from the thermodynamic calculation assuming equilibrium evaporation and with no kinetic barrier ($\eta_v = 1$). Evaporation results of this study confirm that forsterite is much more refractory under kinetic evaporation conditions than expected from thermodynamic considerations alone, in agreement with Hashimoto's analysis (1990). The study of evaporation kinetics thus not only provides a time scale for chemical fractionation in the early solar nebula but also gives new meaning to the term "refractory". Evaporation kinetics must be taken into account when studying chemical and isotopic fractionation between gas and a condensed phase.

3.2. Mg Diffusion and Mg Isotopic Fractionation

Figure 2 shows one of the $\delta^{26}\text{Mg}$ profiles obtained from unevaporated forsterite. Each point in the diagram is the average of five scans. The standard deviation for this whole set of 20 data points (100 scans collected for 5.5 h with a primary

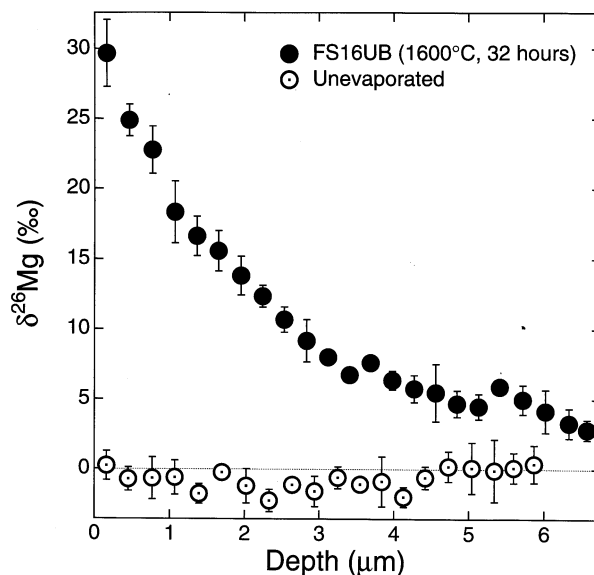


Fig. 2. The $\delta^{26}\text{Mg}$ of a forsterite evaporation residue versus depth from the evaporating surface. The unevaporated forsterite sample shows a constant magnesium isotope composition. FS16UB is from the run FS16 residue (1600°C, 32 h).

beam of 60 nA) is $\pm 1.3\text{‰}$ (1σ). Also plotted on the diagram is the $\delta^{26}\text{Mg}$ profile in the residue of forsterite evaporated at 1600°C for 32 h. All evaporation experiments except FS13 and FS14 were long enough and the chips of the forsterite were thick enough that steady-state isotope profiles were produced near the evaporating surface and the magnesium isotopic composition of the inner portion of the residue was not disturbed.

According to the model discussed in Appendix A, by plotting $\ln \delta^{26}\text{Mg}$ (relative to the starting material) versus depth from the evaporating surface, the diffusion coefficient for Mg can be obtained from the slope ($-v/D$), and the isotopic fractionation factor of magnesium between solid forsterite and its gas phase species from the intercept ($\ln 1000(\alpha - 1)$). Figure 3 is one such plot, from the profile collected from forsterite residue FS2 (1750°C for 1 h). The inferred values of the diffusion coefficient and Mg isotopic fractionation factor for each evaporation experiment are given in Table 2 and the averages at each temperature are given in Table 4. The uncertainty given is the one sigma standard deviation among different analyses.

Figure 4 shows the temperature dependence of the diffusion coefficient of Mg in forsterite along the a -axis. The D_0 and E_D deduced from this plot are 1.32×10^6 cm^2 s^{-1} and 608 kJ mole^{-1} , respectively, for the temperature range of 1500 to 1800°C (Table 4). These results are slightly different from our early report of 5.23×10^6 cm^2 s^{-1} and 630 kJ mole^{-1} (Wang et al., 1993) due to the previous inclusion of data from non-flat-bottom ion-sputtered craters. Morioka (1981) reported values of 1.54×10^3 cm^2 s^{-1} and 444 kJ mole^{-1} for 1300–1400°C for magnesium diffusion in forsterite along the c -axis. Hallwig et al. (1980) reported values of 2.14 cm^2 s^{-1} and 366 kJ mole^{-1} for 1100–1425°C for magnesium diffusion in forsterite. Chakraborty et al. (1994) reported values of 9.6 cm^2 s^{-1} and 400 ± 60 kJ mole^{-1} for 1000–1300°C for magnesium diffusion in forsterite along the c -axis at an oxygen fugacity of

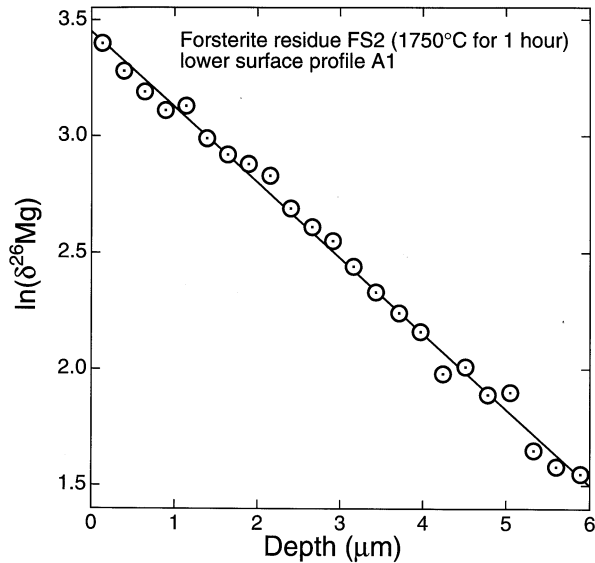


Fig. 3. Plot of $\ln \delta^{26}\text{Mg}$ versus the distance from the evaporating surface. From the linear fit to the data, the diffusion coefficient of magnesium in the synthetic forsterite along the a -axis was found to be $3.23 \times 10^{-10} \text{ cm}^2 \text{ s}^{-1}$ and the fractionation factor for $^{26}\text{Mg}/^{24}\text{Mg}$ between the forsterite crystal and the evaporating gas, 1.0315. The fitting coefficient to the data is 0.994.

10^{-12} atm. They also found that at 1100°C the diffusivity along the c -axis was four times faster than along the a -axis and six times faster than along the b -axis. If the literature data are extrapolated to the temperatures of our experiments (Table 5), their diffusion coefficients are 2–21 (Hallwig et al., 1980), 17–76 (Morioka, 1981), and 0.33–2.3 (Chakraborty et al., 1994) times greater than results from 1800 to 1500°C of this study. Previous work on cation diffusion in olivine and forsterite revealed that cations diffuse faster parallel to the c -axis than parallel to the a - and b -axes. Anisotropy in diffusion rates usually decreases at higher temperatures, especially close to the melting point. Our preliminary work on magnesium diffusion along the c -axis of the forsterite crystal indicates that there is not much anisotropy in diffusivity in the temperature range 1650 – 1800°C .

Hallwig et al. (1980) used electron beam evaporation to deposit ^{26}Mg -enriched Mg_2SiO_4 onto the surface of an iso-

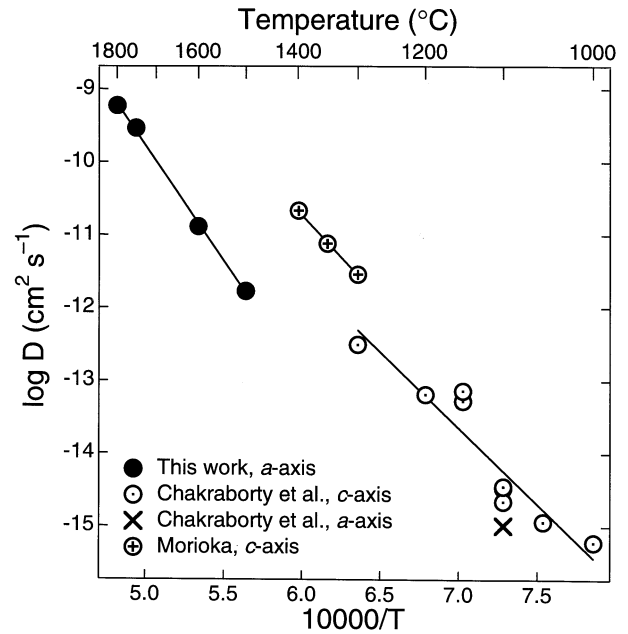


Fig. 4. Plot of magnesium diffusion coefficient along a -axis in forsterite versus temperature. The line is a linear fit to the data which gives an activation energy (E_D) for the magnesium diffusion of $608 \pm 30 \text{ kJ mole}^{-1}$ and a preexponential quantity (D_0) of $1.32 \times 10^6 \text{ cm}^2 \text{ s}^{-1}$.

pically normal crystal of Mg_2SiO_4 . Diffusion of the ^{26}Mg into the forsterite crystal was carried out in air at atmospheric pressure. They determined the magnesium diffusion coefficient in forsterite by comparing the ^{24}Mg change on the sample surface during annealing to solutions of the diffusion equation. Since very few details of this technique were given in their extended abstract (Hallwig et al., 1980), it is extremely difficult to evaluate the accuracy of their results. Their technique requires precise measurement not only of the amount of ^{26}Mg -enriched Mg_2SiO_4 deposited on the sample surface, but also of the surface ^{26}Mg concentration after annealing. Information on these aspects is needed to further compare their results with those of the present study.

Morioka (1981) deposited a thin layer of ^{26}MgO on a forsterite crystal by evaporation from a dilute HNO_3 solution. He used an ion microprobe with a primary beam size of $3 \mu\text{m}$ to

Table 4. Magnesium diffusion along a -axis and magnesium isotopic fractionation in forsterite.

Temperature ($^\circ\text{C}$)	Diffusion coefficient ($\text{cm}^2 \text{ s}^{-1}$)				α^* This study
	Hallwig [†]	Morioka [‡]	Chakraborty [§]	This study	
1500	3.52×10^{-11}	1.28×10^{-10}	3.92×10^{-12}	1.69×10^{-12}	1.0259
1600	1.33×10^{-10}	6.38×10^{-10}	1.67×10^{-11}	$1.33 \pm 0.23 \times 10^{-11}$	1.0280 ± 0.0019
1700	7.58×10^{-10}	5.28×10^{-9}	1.12×10^{-10}	$2.96 \pm 0.43 \times 10^{-10}$	1.0317 ± 0.0028
1800	1.28×10^{-9}	9.99×10^{-9}	1.99×10^{-10}	$5.99 \pm 0.81 \times 10^{-10}$	1.0280 ± 0.0029
Average					1.0294 ± 0.0030

From our diffusion data, we obtain $D_0 = 1.32 \times 10^6 \text{ cm}^2 \text{ s}^{-1}$ and $E_D = 608 \pm 30 \text{ kJ mole}^{-1}$.

* $\alpha = [(^{26}\text{Mg}/^{24}\text{Mg})_{\text{solid}} / (^{26}\text{Mg}/^{24}\text{Mg})_{\text{gas}}]$. [†] Extrapolated from the data of Hallwig et al. (1980). [‡] Extrapolated from the c -axis data of Morioka (1981). [§] Extrapolated from the c -axis data of Chakraborty et al. (1994), and multiplied by a factor of 4 (their measured ratio of the a -axis diffusivity over c -axis diffusivity at 1100°C).

measure $^{26}\text{Mg}/^{24}\text{Mg}$ ratios in a series of spots in a cross section of the annealed forsterite. He obtained magnesium diffusion coefficients in forsterite by comparing the measured profiles with a diffusion equation. It is crucial to determine accurately the position of the ^{26}MgO and forsterite interface before reliable diffusion data can be obtained. Morioka (1981) counted ^{28}Si intensities at the same time as measuring the ^{26}Mg and he defined the interface to be the point where the ^{28}Si intensity was half that of the level-off (maximum) intensity. In the example he gave, his determined interface was $>15\ \mu\text{m}$ away from the level-off point and accounted for more than one-third of the diffusion depth of $<45\ \mu\text{m}$. As pure forsterite (as opposed to a mixture of forsterite and the mounting medium) should begin at the level-off point ($\pm 3\ \mu\text{m}$ due to beam size), this assignment of the interface overestimates the diffusion depth and thus the diffusion coefficient. Recalculation of Morioka's data using the level-off point as the interface gave a diffusion coefficient about eight times smaller than he obtained. If magnesium diffusion at 1350°C is 10 times slower along the a -axis than along the c -axis due to anisotropy, the newly estimated diffusion coefficient of magnesium from Morioka's data ($1.0 \times 10^{-13}\ \text{cm}^2\ \text{s}^{-1}$) is only about three times faster than that extrapolated from this study ($4.2 \times 10^{-14}\ \text{cm}^2\ \text{s}^{-1}$).

Chakraborty et al. (1994) evaporated a dilute HCl solution of ^{26}MgO onto the surface of polished synthetic forsterite. They also tried HNO_3 solutions, but found that nitric acid corroded the surface of the forsterite. After the runs, magnesium isotope profiles were measured by depth profiling with an ion microprobe. Their data covers a fairly wide range of temperatures, from 1000 to 1300°C . Most of the Chakraborty et al. runs measured diffusion parallel to the c -axis, although they did one run at 1100°C with diffusion parallel to the a -axis. Their c -axis data do not extrapolate to our 1500°C a -axis point, but, taking into account the apparent slower diffusion along the a -axis, the Chakraborty et al. data appear to be in good agreement with ours. The change in slope between the two data sets suggests a change in the mechanism of magnesium self-diffusion in forsterite.

The magnesium isotopic fractionation factors α in Table 4 do not show any systematic trend with respect to temperature within the analytical precision, which is in agreement with the observation of Davis et al. (1990). This confirms that the observed isotopic fractionation is a result of a temperature-independent kinetic effect. The average fractionation factor for $^{26}\text{Mg}/^{24}\text{Mg}$ between forsterite crystal and its gas species is 1.0294 ± 0.0006 during the kinetic evaporation process. This is smaller than the ideal kinetic fractionation factor of 1.041 for magnesium evaporating as Mg atoms, but it is very close to the value measured for evaporation of liquid Mg_2SiO_4 , 1.0314 (Davis et al., 1990). Reprecipitation of the evaporated species on the crystal surface would reduce the measured fractionation factor. The amount of reprecipitation depends on sample area. The largest sample had an area of $2.7\ \text{cm}^2$, which would lead to 27% reprecipitation and is enough to explain the discrepancy. However, most other samples were significantly smaller and we see no correlation between sample surface area and the isotopic fractionation factor. A second consideration is that large amounts of forsterite were evaporated in many runs, and may have completely covered the inner surface of the heat shield with condensed forsterite. Upon heating in later experiments, it

is possible that this forsterite would evaporate at some rate. Since the surface area of the heat shield is large, even a relatively low evaporation rate might make a significant contribution to the effective recondensation rate. Arguing against this is the observation that there is no correlation of fractionation factor with temperature (the evaporation rate of forsterite from the radiation shield should increase with temperature). We do note that the average fractionation factor is 1.0323 ± 0.0009 for runs FS2, FS3, and FS4, and 1.0280 ± 0.0005 for all later runs. Thus, although reprecipitation may have played a role in reducing the fractionation factor, it may not explain the entire difference between measured values and the value expected for magnesium evaporating as Mg atoms. Another alternative is exchange between the sample surface and the evaporating gas, which has a similar effect on reducing the measured magnesium isotopic fractionation factor. When the reprecipitation factor was considered, an upper limit of the condensation coefficient η_c of 0.5 was used. Although $>50\%$ of the gas that collided with the sample surface did not precipitate, it could exchange with the sample and lower the measured fractionation factor. Twenty-eight percent of such exchange is required to produce the observed average $^{26}\text{Mg}/^{24}\text{Mg}$ fractionation factor based on the evaporation of $\text{Mg}_{(\text{gas})}$. The average area of samples used to calculate the average $^{26}\text{Mg}/^{24}\text{Mg}$ fractionation factor is $3.0\ \text{cm}^2$, implying that, on average, 30% of the gas evaporated from the surface could return to collide with the sample surface. However, we do not believe that isotopic exchange can explain the difference between the measured $^{26}\text{Mg}/^{24}\text{Mg}$ fractionation factor and that calculated for evaporation of $\text{Mg}_{(\text{gas})}$, for two reasons: (1) there is no correlation between sample surface area and $^{26}\text{Mg}/^{24}\text{Mg}$ fractionation factor; and (2) it is unlikely that every Mg atom striking the surface undergoes an exchange reaction.

Another possibility for the diminished $^{26}\text{Mg}/^{24}\text{Mg}$ fractionation factor is that other species with higher molecular weight, such as MgO ($\alpha = 1.0247$), were involved in evaporation. The previous section showed that the calculated rate for evaporation reaction IV is smaller than but very close to the experimentally determined evaporation rate of forsterite. It is very attractive to resort to this evaporation reaction to solve two problems at the same time. If both evaporation reactions I and IV occur in parallel, then the observed evaporation rate requires an average of 74% of reaction involving $\text{MgO}_{(\text{gas})}$ (IV), and the magnesium isotopic fractionation requires 71% of that reaction. These two numbers are not significantly different, considering the errors related to the measurement of either evaporation rate or the fractionation factor. Recent measurements of the gas phase species resulting from Langmuir evaporation of forsterite indicate that the dominant gas phase species are Mg, SiO, O, and O_2 (Nichols et al., 1998).

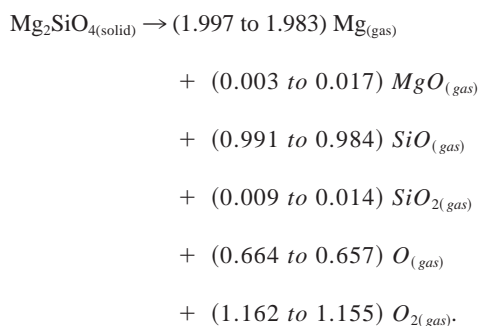
Another point to be stressed is the application of isotopic fractionation profiles in detecting evaporation history. If our experimental evaporation rate and diffusion coefficient can be extrapolated down to 1400°C , it would take ≥ 35 days for the magnesium isotopic fractionation to reach a steady state profile of about $10\ \mu\text{m}$. On the other hand, if diffusivity increases by >10 times, as other workers measured at lower temperatures (Hallwig et al., 1980; Morioka, 1981), although the extrapolated evaporation rate is still valid, it would then take about 350 days to get a profile of $100\ \mu\text{m}$. It is then possible to detect

evaporation residues in meteoritic materials using magnesium isotopic distributions in forsterite.

4. CONCLUSIONS

The evaporation of solid forsterite supports our model of isotopic fractionation under diffusion-controlled conditions (Appendix A), such that isotopic fractionation during the evaporation process is restricted to the vicinity of the evaporating surface. Evaporation does not necessarily result in measurable, mass-dependent kinetic isotopic fractionation in the whole evaporation residue. The limit of our ability to detect isotopic fractionation in meteoritic materials should not be used as evidence to rule out the evaporation origin of these materials.

The evaporation of single crystal forsterite revealed that the evaporation process is kinetically hindered. The thermodynamically most probable evaporation reactions of forsterite from 1500 to 1800°C, from which the maximum evaporation rates J_e were calculated, are:



The activation energy of forsterite evaporation obtained from this study is 619 kJ mole⁻¹, while the activation energy of the thermodynamically most probable evaporation reaction is 503 kJ mole⁻¹. Forsterite can thus be much more refractory at low temperatures than expected from thermodynamic predictions.

Magnesium isotopic fractionation during the evaporation of solid forsterite can be predicted using our theoretical model. The measured solid-gas fractionation factor of ²⁶Mg/²⁴Mg is smaller than the theoretical prediction, suggesting more complicated gas speciation than the simple Mg gas. This fractionation factor is similar to that observed during the evaporation of liquid Mg₂SiO₄ (Davis et al., 1990) and solar composition melt (Wang et al., 1994b; Wang, 1995), which implies that magnesium evaporation involves similar species. Diffusion coefficients of magnesium (interchange mechanism) at high temperature (1500–1800°C) were obtained based on our model and isotopic measurement of forsterite evaporation residues. Magnesium diffusion in forsterite along its crystallographic *a*-axis has a very high activation energy (608 kJ/mole).

Acknowledgments—This research was supported by the National Aeronautics and Space Administration, through grants NAGW-3345 and NAGW-3069 (to RNC), NAGW-3384 (to AMD), and NAG9-28 (to J. A. Wood), and the Smithsonian Institution Scholarly Studies Program, through grant SS72-3-86 (to J. A. Wood). We are grateful to Dr. Robert C. Morris of Allied-Signal, Inc. for providing us with the single crystal forsterite used in our experiments. The first author would like to thank Zhenwei Qin for his advice in finding the analytical solution to the model of isotopic fractionation during the evaporation process.

REFERENCES

- Albarède F. and Bottinga Y. (1972) Kinetic disequilibrium in trace element partitioning between phenocrysts and host lava. *Geochim. Cosmochim. Acta* **36**, 141–156.
- Banner A. E. and Stimpson B. P. (1974) A combined ion probe/spark source analysis system. *Vacuum* **24**, 511–517.
- Bearman R. J. and Jolly D. L. (1981) Mass dependence of the self diffusion coefficients in two equimolar binary liquid Lennard-Jones systems determined through molecular dynamics simulation. *Molec. Phys.* **44**, 665–675.
- Bigeleisen J. (1948) Isotopic exchange reactions and chemical kinetics. *B.N.L. U.S. Rep.* **C8**, 70.
- Bigeleisen J. (1949) The relative reaction velocities of isotopic molecules. *J. Chem. Phys.* **17**, 675–678.
- Bigeleisen J. and Mayer M. G. (1947) Calculation of equilibrium constants for isotopic exchange reactions. *J. Chem. Phys.* **15**, 261–276.
- Buening D. K. and Buseck P. R. (1973) Fe-Mg lattice diffusion in olivine. *J. Geophys. Res.* **78**, 6852–6862.
- Carslaw H. S. and Jaeger J. C. (1959) *Conduction of Heat in Solids*. Clarendon Press.
- Chakraborty S., Farver J. R., Yund R. A., and Rubie D. C. (1994) Mg tracer diffusion in synthetic forsterite and San Carlos olivine as a function of P, T and fO₂. *Phys. Chem. Minerals* **21**, 489–500.
- Chase M. W. Jr., Davies C. A., Downey J. R. Jr., Frurip D. J., McDonal R. A., and Syverud A. N. (1985) JANAF thermodynamical tables, 3rd ed., *J. Phys. Chem. Ref. Data* **14**, Suppl. 1.
- Chou C.-L., Baedeker P. L., and Wasson J. T. (1976) Allende inclusions: Volatile-element distribution and evidence for incomplete volatilization of precursor solids. *Geochim. Cosmochim. Acta* **40**, 85–94.
- Clark A. M. and Long J. V. P. (1971) The anisotropic diffusion of nickel in olivine. In *Proceedings of the Thomas Graham Memorial Symposium on Diffusion Processes* (eds. J. N. Sherwood et al.), pp. 511–521. Gordon and Breach.
- Clayton R. N., Hinton R. W., and Davis A. M. (1988) Isotopic variations in the rock-forming elements in meteorites. *Phil. Trans. R. Soc. Lon.* **A 325**, 483–501.
- Crank J. (1984) *Free and Moving Boundary Problems*. Clarendon Press.
- Davis A. M., Hashimoto A., Clayton R. N., and Mayeda T. K. (1990) Isotope mass fractionation during evaporation of Mg₂SiO₄. *Nature* **347**, 655–658.
- Durham W. B., Froidevaux C., and Jaoul O. (1979) Transient and steady-state creep of pure forsterite at low stress. *Phys. Earth Planet. Inter.* **19**, 263–274.
- Dushman S. (1961) *Scientific Foundations of Vacuum Technique*, 2nd edition. Wiley.
- Eberhardt A., Delwiche R., and Geiss J. (1964) Isotopic effects in single filament thermal ion sources. *Z. Naturforsch.* **19a**, 736–740.
- Hallwig D., Schachtner R., and Sockel H. G. (1980) Diffusion of magnesium, silicon and oxygen in Mg₂SiO₄ and formation of the compound in the solid state. In *Reactivity of Solids* (eds K. Dyrek et al.), pp. 166–169.
- Hashimoto A. (1983) Evaporation metamorphism in the early solar nebula—evaporation experiments on the melt FeO-MgO-SiO₂-CaO-Al₂O₃ and chemical fractionations of primitive materials. *Geochem. J.* **17**, 111–145.
- Hashimoto A. (1990) Evaporation kinetics of forsterite and implications for the early solar nebula. *Nature* **347**, 53–55.
- Hulme K. F. (1955) On the distribution of impurity in crystals grown from impure unstirred melts. *Proc. Phys. Soc.* **68-B**, 393–399.
- Ireland T. R., Zinner E. K., Fahey A. J., and Esat T. M. (1992) Evidence for distillation in the formation of HAL and related hibonite inclusions. *Geochim. Cosmochim. Acta* **56**, 2503–2520.
- Jambon A. (1980) Isotopic fractionation: A kinetic model for crystal growing from magmatic melts. *Geochim. Cosmochim. Acta* **44**, 1373–1380.
- Jaoul O., Houlier B., and Abel F. (1983) Study of ¹⁸O diffusion in magnesium orthosilicate by nuclear microanalysis. *J. Geophys. Res.* **88**, 613–624.
- Jaoul O., Froidevaux C., Durham W. B., and Michaut M. (1980)

- Oxygen self-diffusion in forsterite: Implications for the high-temperature creep mechanism. *Earth Planet. Sci. Lett.* **47**, 391–397.
- Jaoul O., Poumellec M., Froidevaux C., and Havette A. (1981) Silicon diffusion in forsterite: A new constraint for understanding mantle deformation. In *Anelasticity in the Earth* (eds F. D. Stacey and M. S. Paterson), 95–100. Amer. Geophys. Union.
- Knudsen M. (1909) Die Molekularströmung der Gase durch Öffnungen und die Effusion. *Ann. Phys.* 4th series **28**, 999–1016.
- Kurat G. (1970) Zur Genese der Ca-Al-reichen Einschlüsse im Chondriten von Lancé. *Earth Planet. Sci. Lett.* **9**, 225–231.
- Lantelme F. (1982) Mass and size effect in condensed fluids: Rare gases and ionic liquids. *Molec. Phys.* **47**, 1277–1284.
- Langmuir I. (1913) The vapor pressure of metallic tungsten. *Phys. Rev.* 2nd series **2**, 329–342.
- Lee T., Russell W. A., and Wasserburg G. J. (1979) Calcium isotopic anomalies and the lack of aluminum-26 in an unusual Allende inclusion. *Astrophys. J. Lett.* **228**, L93–L98.
- Manning J. R. (1974) Diffusion kinetics and mechanisms in simple crystals. In *Geochemical Transport and Kinetics* (eds. A. W. Hofmann et al.), 3–13. Carnegie Inst. Washington.
- Molini-Velsko C., Mayeda T. K., and Clayton R. N. (1987) Silicon isotope systematics during distillation. *Lunar Planet. Sci.* **18**, 657–658.
- Morioka M. (1980) Cation diffusion in olivine—I. Cobalt and magnesium. *Geochim. Cosmochim. Acta* **44**, 759–762.
- Morioka M. (1981) Cation diffusion in olivine—II. Ni-Mg, Mn-Mg, Mg and Ca. *Geochim. Cosmochim. Acta* **45**, 1573–1580.
- Mysen B. O. and Kushiro I. (1988) Condensation, evaporation, melting, and crystallization in the primitive solar nebula: Experimental data in the system MgO-SiO₂-H₂ to 1.0 × 10⁻⁹ bar and 1870°C with variable oxygen fugacity. *Amer. Mineral.* **73**, 1–19.
- Nagahara H., Kushiro I., Mysen B. O., and Mori H. (1988) Experimental vaporization and condensation of olivine solid solution. *Nature* **331**, 516–518.
- Nagahara H., Kushiro I., and Mysen B. O. (1994) Evaporation of olivine: Low pressure phase relations of the olivine system and its implication for the origin of chondritic components in the solar nebula. *Geochim. Cosmochim. Acta* **58**, 1951–1963.
- Nagahara H. and Ozawa K. (1996) Evaporation of forsterite in H₂ gas. *Geochim. Cosmochim. Acta* **60**, 1445–1459.
- Nagasawa H. and Onuma N. (1979) High temperature heating of the Allende meteorite II. *Lunar Planet. Sci.* **10**, 884–886.
- Nichols R. H. Jr., Grimley R. T., and Wasserburg G. J. (1998) Measurement of gas-phase species during Langmuir evaporation of forsterite (abstract). *Meteoritics and Planet. Sci.* **33**, A115–A116.
- Niederer F. R. and Papanastassiou D. A. (1984) Ca isotopes in refractory inclusions. *Geochim. Cosmochim. Acta* **48**, 1279–1293.
- Notsu K., Onuma N., Nishida N., and Nagasawa H. (1978) High temperature heating of the Allende meteorite. *Geochim. Cosmochim. Acta* **42**, 903–907.
- Rayleigh J. W. S. (1896) Theoretical considerations respecting the separation of gases by diffusion and similar processes. *Philos. Mag.* **42**, 493–498.
- Rees C. E. (1969) Fractionation effects in the measurement of molybdenum isotope abundance ratios. *Int. J. Mass Spectrom. Ion Phys.* **3**, 71–80.
- Rutner E. (1962) Some limitations on the use of the Langmuir and Knudsen techniques for determining kinetics of evaporation. In *Condensation and Evaporation of Solids* (eds E. Rutner et al.), pp. 149–163. Gordon and Breach.
- Ryerson F. J., Durham W. B., Cherniak D. J., and Lanford W. A. (1989) Oxygen diffusion in olivine: Effect of oxygen fugacity and implications for creep. *J. Geophys. Res.* **94**, 4105–4118.
- Scatena-Wachel D. E. (1986) Ion microprobe measurements of radiogenic nuclides: Cosmochemical and geochemical tracers. Ph. D. dissertation, Univ. Chicago.
- Sentfle F. E. and Bracken J. T. (1955) Theoretical effect of diffusion on isotopic abundance ratios in rocks and associated fluids. *Geochim. Cosmochim. Acta* **7**, 61–76.
- Smith V. G., Tiller W. A., and Rutter J. W. (1955) A mathematical analysis of solute redistribution during solidification. *Canad. J. Phys.* **33**, 723–745.
- Tanaka T. and Masuda A. (1973) Rare-earth elements in matrix, inclusions, and chondrules of the Allende meteorite. *Icarus* **19**, 523–530.
- Tiller W. A., Jackson K. A., Rutter J. W., and Chalmers B. (1953) The redistribution of solute atoms during the solidification of metals. *Acta Metall.* **1**, 428–437.
- Tilles D. (1961) Natural variations in isotopic abundances of silicon. *J. Geophys. Res.* **66**, 3003–3013.
- Tsuchiyama A., Kawamura K., Nakao T., and Uyeda C. (1994) Isotopic effects on diffusion in MgO melt simulated by the molecular dynamics (MD) method and implications for isotopic mass fractionation in magmatic systems. *Geochim. Cosmochim. Acta* **58**, 3013–3021.
- Urey H. C. (1947) The thermodynamic properties of isotopic substances. *J. Chem. Soc.* 562–581.
- Uyeda C., Tsuchiyama A., and Okano J. (1991) Magnesium isotopic fractionation of silicates produced in condensation experiments. *Earth Planet. Sci. Lett.* **107**, 138–147.
- Wang J. (1995) Chemical and isotopic fractionation during the evaporation of synthetic forsterite and material of solar composition. Ph. D. dissertation, Univ. Chicago.
- Wang J., Davis A. M., and Clayton R. N. (1994a) Modeling of isotopic fractionation during the phase transition of a diffusion-controlled reservoir. *USGS Circular* **1107**, 348.
- Wang J., Davis A. M., Clayton R. N., and Mayeda T. K. (1994b) Chemical and isotopic fractionation during the evaporation of FeO-MgO-SiO₂-CaO-Al₂O₃-TiO₂-REE melt system. *Lunar Planet. Sci.* **25**, 1457–1458.
- Wang J., Davis A. M., Clayton R. N., and Mayeda T. K. (1994c) Kinetic isotopic fractionation during the evaporation of the iron oxide from liquid state. *Lunar Planet. Sci.* **25**, 1459–1460.
- Wang J., Davis A. M., Hashimoto A., and Clayton R. N. (1991) The role of diffusion in the isotopic fractionation of magnesium during the evaporation of forsterite. *Lunar Planet. Sci.* **22**, 1461–1462.
- Wang J., Davis A. M., Hashimoto A., and Clayton R. N. (1993) Diffusion-controlled magnesium isotopic fractionation of a single crystal forsterite evaporated from the solid state. *Lunar Planet. Sci.* **24**, 1479–1480.

APPENDIX A

Evaporation and condensation processes can occur under either equilibrium or disequilibrium (kinetically-controlled) conditions. Isotopic fractionation can result from either a thermodynamic equilibrium process due to different vibration-rotation energy levels of the isotopes in the two phases (Urey, 1947; Bigeleisen and Mayer 1947), or a kinetic process due to different transport properties of the isotopes (Bigeleisen, 1948, 1949). The equilibrium effect is both mass- and temperature-dependent and decreases with the increase of mass and/or temperature. On the other hand, isotopic fractionation during the kinetic evaporation process is mass-dependent only and may be independent of temperature. At high temperatures, the equilibrium fractionation effects for elements such as magnesium, silicon, calcium, and titanium are insignificant relative to the kinetic effects. In our model, the equilibrium effect will be neglected and only the kinetic isotopic fractionation effect will be considered. Kinetic evaporation of a solid or liquid residue involves two processes: (1) transport of isotopes from the residue to the gas phase, and (2) transport of isotopes within the residue. Our previous knowledge of isotopic fractionation during the evaporation process is mainly from the Rayleigh distillation law that deals only with the kinetic aspect of the transformation of the residue to the gas. The present modeling effort is intended to incorporate into the system the kinetic aspect of transport of isotopes within the residue.

Diffusion Kinetics

The transport of isotopes within the residue involves two aspects of diffusion: self-diffusion of the element and self-diffusion of individual isotopes. Bearmann and Jolly (1981) indicated that diffusivity D is proportional to $1/m^\sigma$ (where m is the mass of an isotope and $\sigma \leq 0.5$), indicating that self-diffusion coefficients for different isotopes can be different. Lantelme (1982) used molecular dynamics (MD) to calculate σ for the melts of noble gases and alkali halides and found that it ranged from 0.065 to 0.25. Using MD calculations, Tsuchiyama et al.

(1994) found that self-diffusion coefficients of magnesium and oxygen isotopes in an MgO melt have a mass dependent index σ of roughly 0.1. This index should generally be smaller in crystalline material. In the crystal case (due to stoichiometric requirements), lattice diffusion of different isotopes of a major element is governed by interdiffusion of different isotopes rather than by their self-diffusion rates. This means that the slowest diffusing isotope (the heaviest) of the studied element limits the self-diffusion of different isotopes during lattice diffusion within the crystal. Even for the melt case, the differential diffusion rates between different isotopes are so small that isotopic fractionation in the melt due to diffusion process is insignificant (Senthle and Bracken, 1955; Jambon, 1980; Tsuchiyama et al., 1994) compared with the kinetic evaporation process. In the present model, we will consider only the self-diffusion of an element in the system.

Evaporation Kinetics

In a gas-liquid or gas-solid system, Knudsen (1909) and Langmuir (1913) showed that the rate (J) at which gas molecules collide with the surface of the condensed phase (liquid or solid) is

$$J = \frac{n}{V} u = \left(\frac{P}{kT} \right) \frac{1}{2} \sqrt{\frac{2kT}{\pi m}} = \frac{P}{\sqrt{2\pi m kT}}, \quad (\text{A1})$$

where n is the number of gas molecules, u is the average molecular speed toward the surface in the x direction normal to it, V is the volume of the gas, P is the gas pressure, k is the Boltzmann constant, T is the temperature in Kelvin, and m is the mass of a gas molecule. For an ideal gas at equilibrium, the pressure P can be obtained from thermodynamic data. If all the gas molecules that collide on the surface condense, the evaporation rate reaches its maximum value and is the same as the condensation rate. Free evaporation occurs when newly formed gas molecules are immediately removed from the system so that no condensation occurs at the evaporating surface. During the free evaporation process, the instantaneous composition of the evaporating gas in terms of the isotopic ratio (R_{gas}) can be obtained as

$$R_{\text{gas}} = \frac{J_{m_2}}{J_{m_1}} = \frac{C_2^{\text{condensed}} P_{\text{total}}}{\sqrt{2\pi m_2 kT}} \div \frac{C_1^{\text{condensed}} P_{\text{total}}}{\sqrt{2\pi m_1 kT}} = \frac{C_2^{\text{condensed}}}{C_1^{\text{condensed}}} \times \sqrt{\frac{M_1}{M_2}}, \quad (\text{A2})$$

where J is the evaporation rate, C is the molar concentration on the evaporating surface in the condensed phase, subscripts 1 and 2 denote molecules containing isotope 1 and 2 respectively, and M_1 and M_2 are the molecular weights of molecules with isotope 1 and 2 respectively. P_{total} is the total thermodynamic equilibrium pressure of the gas containing the two isotopes. If the fractionation factor α is defined as the ratio of isotopic compositions between the condensed phase and the gas phase, then

$$\alpha = \frac{R_{\text{condensed}}}{R_{\text{gas}}} = \frac{C_2^{\text{condensed}}}{C_1^{\text{condensed}}} \div \left(\frac{C_2^{\text{condensed}}}{C_1^{\text{condensed}}} \times \sqrt{\frac{M_1}{M_2}} \right) \Rightarrow \alpha = \sqrt{\frac{M_2}{M_1}}. \quad (\text{A3})$$

This indicates that isotopic fractionation during the free evaporation process is dependent only on the masses of evaporating molecules containing different isotopes. For the case of free evaporation of Mg_2SiO_4 , Hashimoto (1990) found that it evaporates stoichiometrically and that Mg, SiO_2 and O (or O_2) are the rate-controlling gas species. If $R = {}^{26}\text{Mg}/{}^{24}\text{Mg}$ is considered, then the fractionation factor $\alpha = \sqrt{M_2/M_1} = \sqrt{26/24} = 1.0408$. On the other hand, if MgO were the evaporating gas species, then $\alpha = \sqrt{42/40} = 1.0247$. This shows that the isotopic fractionation factor during the kinetic evaporation process depends on the nature of the evaporating gas species. Studies of the isotopic fractionation can thus be used to identify the evaporating species, as we discuss later.

The Semi-infinite Reservoir

A one-dimensional approach is used in the present model and the reservoir is assumed to have a planar evaporating surface. The coordinate of length is perpendicular to the evaporating surface. We will first examine a semiinfinite reservoir as a special case and then the

general case of a reservoir with finite dimensions. Although the model applies to the general situation of isotopic fractionation during evaporation of a reservoir, magnesium isotopic fractionation during the evaporation of forsterite will be used as a specific example to better illustrate the model.

For a semi-infinite reservoir undergoing evaporation, the evaporating surface is kept at the origin ($x = 0$) and the reservoir occupies the entire positive axis. The isotopic ratio $R(x, t)$ is considered as a function of the distance from the evaporating surface (x) in the reservoir and time (t) since the beginning of evaporation. The isotopic composition of the reservoir is initially uniform ($R(x, 0) = R_0$). The isotopes of an element are fractionated at the evaporating surface with a fractionation factor of α . To describe this scenario of isotopic fractionation during evaporation with diffusion in the reservoir involves solving partial differential equations with a moving boundary. There are two sets of equations for separate isotopes related to each other by stoichiometric balance. It is simpler if the isotopic ratio R can be differentiated using simple mass balance equations (Wang, 1995). If the major isotope is used as the denominator to calculate R , R can be differentiated according to a mass balance equation for almost all naturally occurring elements. In other words, the variation of R is due to the change of the numerator rather than that of the denominator. The denominator isotope may be treated as constant and only the numerator isotope is diffusively transported in the reservoir with a diffusion coefficient of D .

Based on the above considerations, the diffusion equation in the reservoir ($0 \leq x \leq X$) can be expressed as

$$\frac{\partial R}{\partial t} = D \frac{\partial^2 R}{\partial x^2} + v \frac{\partial R}{\partial x}, \quad (\text{A4})$$

where v is the evaporation rate of the reservoir. The advection term ($v \partial R / \partial x$) is due to the moving boundary caused by fixing the evaporating surface at the origin. At $x = 0$ (the evaporating surface),

$$D \frac{\partial R}{\partial x} = (R_g - R)v, \quad (\text{A5})$$

where R_g is the isotopic ratio of the gas evaporating from the surface. If R/α is substituted for R_g (by definition), Eq. A5 can be rearranged to yield:

$$D \frac{\partial R}{\partial x} + \beta v R = 0, \quad (\text{A6})$$

where $\beta = (\alpha - 1)/\alpha$. This is the boundary condition at the evaporating surface. Another boundary condition is the isotopic composition at infinity, where the isotopic ratio is constant:

$$R(\infty, t) = R_0. \quad (\text{A7})$$

The initial condition is that the reservoir be homogeneous,

$$R(x, 0) = R_0. \quad (\text{A8})$$

If x and t are nondimensionalized using $X = vx/D$ and $\tau = v^2 t/D$, Eqs. A4, A6, A7, and A8 become

$$\frac{\partial R}{\partial \tau} = \frac{\partial^2 R}{\partial X^2} + \frac{\partial R}{\partial X}, \quad (\text{A9})$$

$$\frac{\partial R(0, \tau)}{\partial X} + \beta R(0, \tau) = 0, \quad (\text{A10})$$

$$R(\infty, \tau) = R_0, \quad (\text{A11})$$

and

$$R(X, 0) = R_0. \quad (\text{A12})$$

Using the Laplace transform, this set of partial differential equations can be solved analytically (Wang, 1995). The solution is as follows:

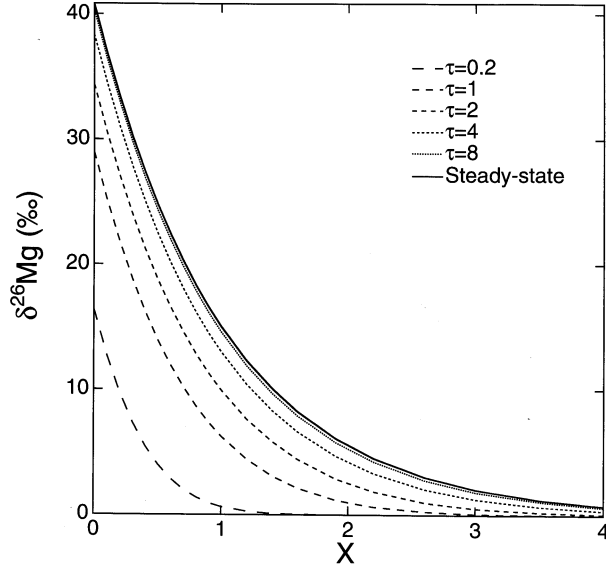


Fig. A1. The results of theoretical modeling showing the profile of magnesium isotopic fractionation ($\delta^{26}\text{Mg}$) in the forsterite residue at different nondimensionalized time τ .

$$\frac{R(X, \tau)}{R_0} = 1 - \frac{1}{2} \operatorname{erfc} \left[\frac{X + \tau}{2\sqrt{\tau}} \right] + \frac{\alpha - 1}{2} e^{-X} \operatorname{erfc} \left[\frac{X - \tau}{2\sqrt{\tau}} \right] + \frac{2 - \alpha}{2} e^{(1-\alpha)(\alpha X + \tau)/\alpha^2} \operatorname{erfc} \left[\frac{\alpha X + (2 - \alpha)\tau}{2\alpha\sqrt{\tau}} \right]. \quad (\text{A13})$$

A similar solution was obtained for the study of solute redistribution during solidification (Smith et al., 1955), distribution of an impurity during crystal growth (Hulme, 1955), and heat conduction with a moving boundary (Carslaw and Jaeger, 1959, p. 389). Albarède and Bottinga (1972) applied a solution of this type to trace element partitioning between phenocrysts and host lava. Jambon (1980) used a similar model for isotopic fractionation in crystals growing from melts. For the case of evaporation of solid forsterite, Fig. A1 illustrates the above result in terms of magnesium isotopic fractionation ($\delta^{26}\text{Mg}$ (‰) = $[(R/R_0) - 1] \times 1000$) profiles in the residue near the evaporating surface for τ values of 0.2, 1, 2, 4, 8 and >10 (steady state). $\delta^{26}\text{Mg}$ at the evaporating surface ($X = 0$) of the forsterite increases with time and approaches a constant value of $(\alpha - 1) \times 1000 = 40.8$. This is the steady state situation, in which the isotopic composition of magnesium leaving the surface of the forsterite crystal equals that deep in the crystal (the same as its initial value). At steady state, the isotopic profile in the reservoir does not change with time, i.e., $\partial R/\partial \tau = 0$. Eqs. A9, A10, A11, and A12 can be easily solved (Wang, 1995) to obtain the following steady state solution:

$$\frac{R(X)}{R_0} = 1 + (\alpha - 1)e^{-X}. \quad (\text{A14})$$

Tiller et al. (1953) used a similar steady state solution to describe solute redistribution during the solidification of metals. If X and τ in Eqns. A12 and A13 are changed to the dimensionalized quantities vX/D and v^2t/D , these equation become

$$\frac{R(x, t)}{R_0} = 1 - \frac{1}{2} \operatorname{erfc} \left[\frac{x + vt}{2\sqrt{Dt}} \right] + \frac{\alpha - 1}{2} e^{-vx/D} \operatorname{erfc} \left[\frac{x - vt}{2\sqrt{Dt}} \right] + \frac{2 - \alpha}{2} e^{(1-\alpha)(\alpha x + vt)/\alpha^2 D} \operatorname{erfc} \left[\frac{\alpha x + (2 - \alpha)vt}{2\alpha\sqrt{Dt}} \right] \quad (\text{A15})$$

and

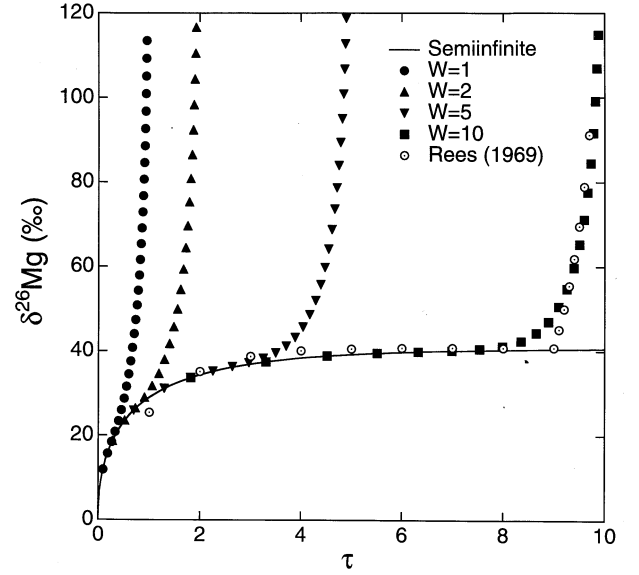


Fig. A2. $\delta^{26}\text{Mg}$ on the surface of evaporating forsterite as a function of time (τ) of evaporation for different initial thicknesses of the reservoir (W). The line labeled “Semiinfinite” is the result of analytical solution for the semiinfinite reservoir.

$$\frac{R(x)}{R_0} = 1 + (\alpha - 1)e^{-vx/D}. \quad (\text{A16})$$

Eq. A16 can be used to obtain both the fractionation factor α (isotopic fractionation between the condensed phase (solid or liquid) and the gas), and the diffusion coefficient D by measuring isotopic profiles in the evaporation residues if the steady state has been reached. This can be achieved by plotting $\ln(R(x)/R_0)$ versus x , where the slope is $-v/D$

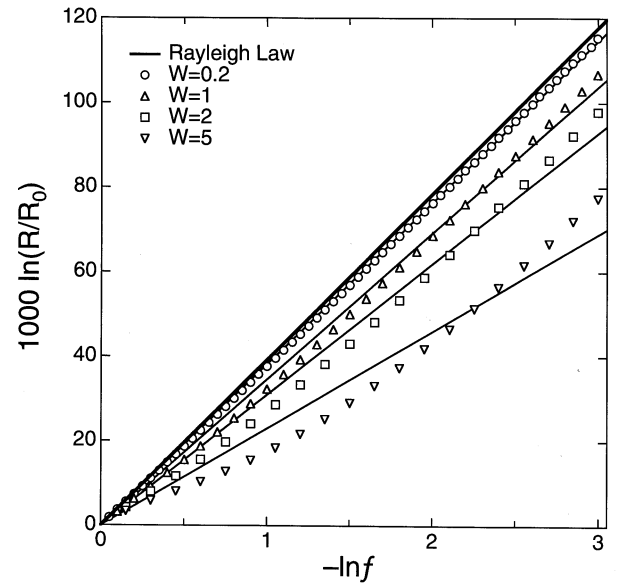


Fig. A3. Bulk $\delta^{26}\text{Mg}$ of the residual forsterite versus the fraction of the original sample that has been evaporated. The line of the Rayleigh Law is also plotted for comparison. Other lines are linear fits to the modeling results (forced through zero).

(v can be obtained from the evaporation experiment) and the intercept is $\ln(\alpha - 1)$, as was done for forsterite evaporation in Fig. 3.

The Finite Reservoir

For a more general case, a diffusion-controlled reservoir with finite thickness w will be examined. By fixing the central plane of the reservoir at $X = 0$ and nondimensionalizing w ($W = vw/D$), Eqs. A9, A10, A11, and A12 can be written as

$$\frac{\partial R}{\partial \tau} = \frac{\partial^2 R}{\partial X^2} \text{ for } 0 \leq X \leq W - \tau \text{ and } \tau > 0, \quad (\text{A17})$$

$$\frac{\partial R(W - \tau, \tau)}{\partial X} - \beta R(W - \tau, \tau) = 0 \text{ for } \tau > 0, \quad (\text{A18})$$

$$\frac{\partial R(0, \tau)}{\partial X} = 0 \text{ for } \tau > 0, \quad (\text{A19})$$

and

$$R(X, 0) = R_0 \text{ for } 0 \leq X \leq W. \quad (\text{A20})$$

Albarède and Bottinga (1972) proposed some numerical schemes to solve similar equations for trace element partitioning between phenocrysts and host lava, but did not solve them. Because they did not fix the crystal-melt surface at the origin and use the implicit method, it is more complicated and difficult to use their scheme. The front-fixing method (cf. Crank, 1984, p. 187) and the Crank-Nicholson implicit scheme were used to solve this set of equations numerically for different initial nondimensionalized thicknesses W in the case of magnesium isotopic fractionation during the evaporation of solid forsterite (Wang, 1995). Figure A2 shows the results for $\delta^{26}\text{Mg}$ on the evaporating surface versus time for different initial thicknesses of the reservoir (W). Also shown on the diagram is a line for the analytical solution for the semiinfinite reservoir for comparison. It can be seen from the diagram that all the numerical results of different initial W fit on the

analytical line in the early stage of evaporation (when τ is relatively small). This indicates that the numerical solution conforms with the analytical solution. Because the numerical result becomes more stable and accurate as τ increases, the isotopic fractionation during the whole evaporation process can be monitored accurately if the analytical solution is applied to the early stage isotopic fractionation.

Rees (1969) combined a semiinfinite model and a Rayleigh law to explain isotopic fractionation in the thermal ionization source of a mass spectrometer. In his illustration for the isotopic fractionation of a solid source with an initial thickness of $10D$ (thickness of the mixed layer), he made a sudden switch from a semiinfinite model to a Rayleigh law for the isotopic fractionation. In order to compare the model of Rees (1969) with the present model, it is assumed that D is the same as W (Fig. A2). It can be seen that the result of Rees' model is approximately the same as the result of a finite reservoir with an initial nondimensionalized size of $10W$ from this study, except that there is a kink at $X = 9W$ in Rees' result. It is apparent that the present model is better defined and more accurate in dealing with isotopic fractionation in thermal ionization mass spectrometry.

In a diffusion-controlled evaporation in which the sample thickness is greater than the diffusion length, it is inappropriate to fit the data to a Rayleigh equation. Figure A3 is a diagram showing $1000\ln(R/R_0)$ (where R is the average $^{26}\text{Mg}/^{24}\text{Mg}$ of the whole remaining forsterite) versus $-\ln f$ (f is the fraction of the initial sample remaining). The Rayleigh fractionation curve is plotted on the diagram for comparison. Linear fits to the modeling results (forced through zero) are also shown. Assuming Rayleigh fractionation, one could mistakenly try to deduce the fractionation factors from the slopes of these fits to experimental data ($1000 - 1000/\alpha$). For small W , such as $W = 0.2$, the results of the present model and the Rayleigh law are similar. One should be cautious in using the Rayleigh law in a system where the nondimensionalized size of the reservoir (W) is large, as Uyeda et al. (1991) did. If τ , X , and W are replaced by dimensional quantities including the evaporation rate v and diffusion coefficient D , this model can be used to deal quantitatively with the experimental situation.